ACS APPLIED MATERIALS & INTERFACES

Research Article

www.acsami.org

Photobias Instability of High Performance Solution Processed Amorphous Zinc Tin Oxide Transistors

Yoon Jang Kim,[†] Bong Seob Yang,[†] Seungha Oh,[†] Sang Jin Han,[†] Hong Woo Lee,[†] Jaeyeong Heo,[‡] Jae Kyeong Jeong,[*,§] and Hyeong Joon Kim[*,†]

[†]Department of Materials Science and Engineering, WCU Hybrid Materials Program, and Inter-university Semiconductor Research Center, Seoul National University, Seoul 151-742, Republic of Korea

[‡]Department of Materials Science and Engineering, Chonnam National University, Gwangju 500-757, Republic of Korea

[§]Department of Materials Science and Engineering, Inha University, Incheon 402-751, Republic of Korea

ABSTRACT: The effects of the annealing temperature on the structural and chemical properties of soluble-processed zinc−tin−oxide (ZTO) films were examined by transmission electron microscopy, atomic force microscopy, high resolution X-ray reflectivity, and X-ray photoelectron spectroscopy. The density and purity of the resulting ZTO channel layer increased with increasing annealing temperature, whereas the oxygen vacancy defect density decreased. As a result, the device performance of soluble ZTO thin film transistors (TFTs) was improved at higher annealing temperature. Although the 300 °C-annealed ZTO TFT showed a marginal field-effect mobility (μ_{FE}) and high threshold voltage (V_{th}) of 0.1 $cm^2/(V\ s)$ and 7.3 V, respectively, the 500 °C-annealed device exhibited a reasonably high μ_{FE}, low subthreshold gate swing (SS), V_{th}, and $I_{on/off}$ of 6.0 $cm^2/(V\ s)$, 0.28 V/decade, 0.58 V, and 4.0 × 10^7, respectively. The effects of dark negative bias stress (NBS) and negative bias illumination stress (NBIS) on the degradation of transfer characteristics of ZTO TFTs were also investigated. The instability of V_{th} values of the ZTO TFTs under NBS and NBIS conditions was suppressed with increasing annealing temperature. To better understand the charge trapping mechanism, the dynamics of V_{th} shift with NBS and NBIS time for all ZTO TFTs was analyzed on the basis of the stretched exponential relaxation. The negative V_{th} shift for each transistor was accelerated under NBIS conditions compared to NBS, which resulted in a higher dispersion parameter and smaller relaxation time for NBIS degradation. The relaxation time for NBS and NBIS instability increased with increasing annealing temperature, which is discussed on the basis of the transition mechanism of oxygen vacancy defects.

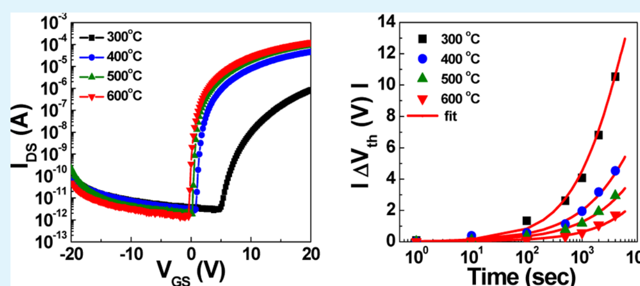

KEYWORDS: *zinc tin oxide (ZTO), soluble process, annealing temperature, thin film transistors (TFTs), bias stress instability, light stress instability*

1. INTRODUCTION

Zinc-based oxide thin film transistors (TFTs) have attracted considerable attention as a switching device for active matrix (AM) liquid crystal displays (LCDs) and organic light-emitting diodes (OLEDs) owing to their high mobility, good transparency to visible light, and low temperature capability compared to amorphous Si TFTs.[1,2] High performance oxide channel layers have been prepared in general by vacuum-based deposition processes, such as sputtering, pulsed laser deposition (PLD), and atomic layer deposition (ALD), which comes with a high manufacturing cost.[3−5] In contrast, solution-processed formation of the oxide layer is a viable alternative, considering its process simplicity, low cost, and high throughput. In addition, direct-writing capabilities of the solution process enable the realization of the low-cost printed electronics for flexible displays and flat panel AM displays. For these reasons, the fabrication of high performance TFTs using solution-based oxide semiconductors, such as InGaZnO,[6,7] InZnO,[8] and InZnSnO,[9] has been studied extensively. Although the use of indium in the active channel layer is believed to be essential for securing high channel mobility, its scarcity in the earth crust and the resulting high price is an obstacle to its widespread utilization in mass-produced printed electronics.[10] In this regard, ZnSnO (ZTO) has been highlighted recently as a desirable active layer owing to its elemental abundance and low cost.

Several studies have examined solution-based ZTO TFTs.[11−16] The device performance of the devices strongly depends on the annealing temperature and the chemistry of the precursors used. Jeong et al. reported the fabrication of ZTO TFTs using zinc acetate dehydrate [$Zn(CH_3COO)_2 \cdot 2H_2O$] and tin acetate [$Sn(CH_3COO)_2$] as the Zn and Sn precursors,

Received: January 23, 2013
Accepted: March 29, 2013
Published: March 29, 2013

 © 2013 American Chemical Society dx.doi.org/10.1021/am400110y | ACS Appl. Mater. Interfaces 2013, 5, 3255−3261

respectively.[12] The transistor performance with a field-effect mobility (μ_{FE}) of 1.1 $cm^2/(V\ s)$ was achieved when the channel layer experienced high-temperature annealing (>500 °C). The formation of the channel layers using the solution process involves the hydrolysis and condensation of molecular precursors, which results in the ionic network of metal−oxygen bonding. The required annealing temperature strongly depends on the precursor structure because the geometrical hindrance and interaction between ligands can affect the sol−gel process during heat treatment.[17−20] In addition, carbon atoms of the acetate-based cation precursors can exist as a residue even after thermal annealing, and it has an adverse effect on the device performance. Therefore, it is beneficial to use carbon-free molecules such as chlorides as metal precursors.[11]

The switching TFTs in LCDs and OLEDs are operated under light from a back light unit and OLEDs. The device stability under the gate bias stress and light stress is an important issue for the implementation of oxide TFTs to the commercial electronic products. Although the effects of the annealing temperature, cation composition, and precursor chemistry on the device performance of soluble processed ZTO TFTs have been investigated in detail, few studies have examined the fundamental relationship between their material properties (e.g., microstructure, density, and impurity) and the photobias instability of the soluble ZTO transistors.

In this paper, high performance solution-processed ZTO TFTs were fabricated using carbon-free $ZnCl_2$ and $SnCl_2$ precursors. The effect of the annealing temperature on the device performance, dark negative bias stress (NBS), and negative bias illumination stress (NBIS) instability was examined on the basis of the structural and chemical characterization of the ZTO films. The relaxation times of V_{th} shift for various ZTO TFTs under NBS and NBIS conditions were also extracted by fitting to a stretched exponential equation, which was found to be strongly dependent on the structural and chemical properties of the soluble-processed ZTO films.

2. EXPERIMENTAL SECTION

The precursor solution was prepared by dissolving 0.1 M $ZnCl_2$ (Aldrich) and $SnCl_2$ (Aldrich) in 10 mL of acetonitrile (CH_3CN, Aldrich). The Zn-to-Sn ratio of the precursors was 1:1. The precursor solution was stirred for 30 min at 60 °C. Heavily doped p-type Si with 100-nm-thick thermally grown SiO_2 gate oxide was used as a substrate for the fabrication of ZTO TFTs. The substrate was sonicated in acetone and isopropanol for 5 min, followed by ultraviolet ozone exposure for 20 min for generating a hydrophilic surface. Spin coating of the ZTO layer was performed at 500 rpm for 5 s and then at 3000 rpm for 30 s. The resulting ZTO film was then dried at 200 °C for 10 min to evaporate the solvent and annealed at temperatures ranging from 300 to 600 °C for 1 h in air. Tin-doped indium oxide (ITO) as source and drain electrodes (S/D) was deposited by dc magnetron sputtering and patterned by a metal shadow mask. The width (W) and length (L) of the fabricated device was 1000 and 300 μm, respectively. Finally, to prevent the dynamic interaction between the channel layer and ambient oxygen/moisture, the fabricated device was encapsulated with polymethyl methacrylate (PMMA, MicroChem A4).

The surface morphology and roughness of the ZTO films were characterized by atomic force microscopy (AFM, JEOL, JSPM-5200) with tapping mode. The structural properties of spin-coated ZTO films were examined by glancing angle X-ray diffraction (GAXRD, PANalytical, X'pert-PRO MPD) and transmission electron microscopy (TEM, FEI, Tecnai F20). The electrical properties of the channel layers were obtained using a Keithley 4200 semiconductor characterization system at room temperature in air. The chemical structure of the ZTO films was evaluated by X-ray photoelectron spectroscopy (XPS, SIGMA PROBE, ThermoVG, U.K.). High-resolution X-ray reflectivity (XRR) was performed to evaluate the roughness, density, and thickness of the ZTO thin films (PANalytical, X'pert-PRO). The XRR data was fitted using the X'pert Reflectivity software package.

3. RESULTS AND DISCUSSION

Thermo-gravimetric analysis (TGA) was performed to monitor the thermal decomposition behavior of ZTO precursor solution, as shown Figure 1. The weight loss observed below 150 °C was attributed to the evaporation of both solvent and organic molecules incorporated into the ZTO solution. The rapid weight loss above 200 °C was attributed to the decomposition of $ZnCl_2$ and $SnCl_2$, which completes at ∼400 °C. Therefore, dense ZTO films form at annealing temperatures higher than 400 °C. Figure 2 shows the XRD patterns of the ZTO films annealed at 300−600 °C. No sharp peak is observed, except for the (311) plane at 54.5° from the Si substrate, indicating that all the annealed films are amorphous. As the annealing temperature increased, the broad hump near 34° emerged slightly. In ZTO systems, trigonal-ilmenite $ZnSnO_3$ was reported to form at relative low temperatures (<600 °C), whereas cubic-spinel Zn_2SnO_4 is formed at high temperatures (>1000 °C).[21] Therefore, the broad peak at 34° was assigned to the (110) diffraction of $ZnSnO_3$, which is the characteristic of the amorphous phase reported previously.[6] The amorphous phase nature of spin-coated ZTO films was confirmed by TEM, as shown in Figure 3a. The amorphous hollow pattern for 300 °C-annealed ZTO film is clearly observed in the selected area diffraction pattern (SADP), as shown in the inset of Figure 3a. In contrast, the ZTO film annealed at 600 °C showed a locally crystallized portion in amorphous matrix, as shown in Figure 3b. The volume fraction of crystallized region to the amorphous ZTO matrix was estimated to be 30−40%. Figure 4 shows AFM images of the

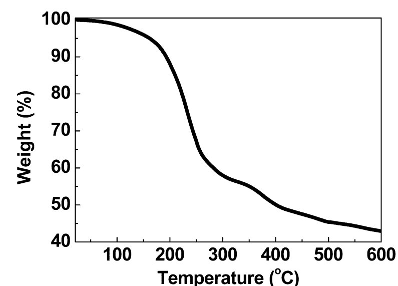

Figure 1. TGA of the ZTO precursor solution at 5 °C min^{-1} heating rate in air.

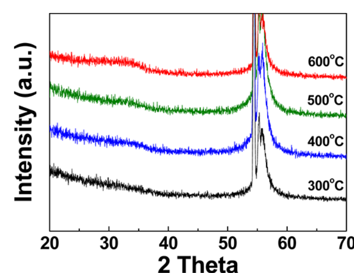

Figure 2. XRD patterns of the ZTO thin films annealed at various temperatures.

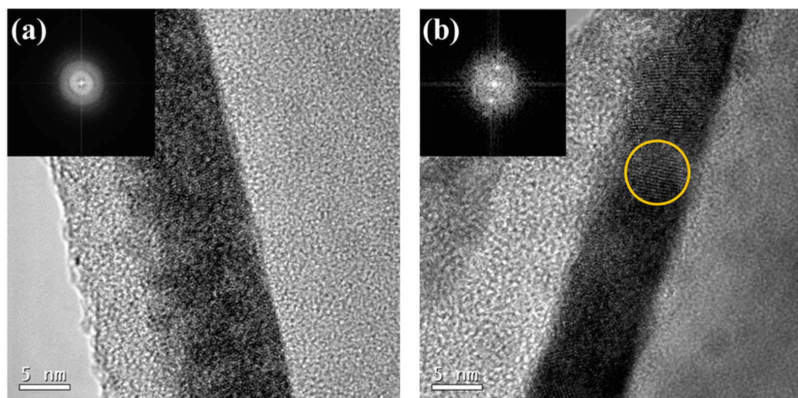

Figure 3. High resolution TEM images of ZTO thin films annealed at (a) 300 and (b) 600 °C.

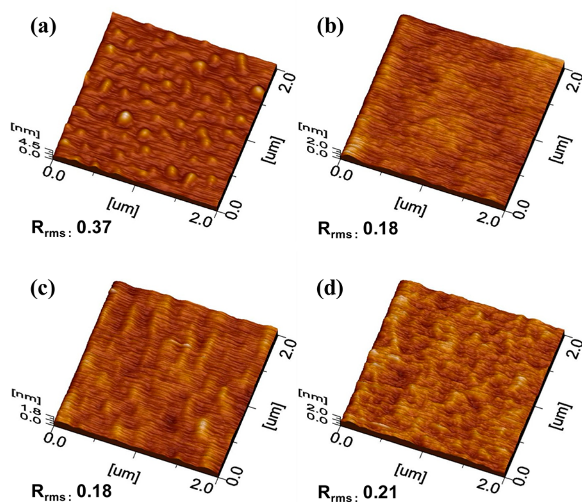

Figure 4. AFM images of the ZTO annealed at (a) 300, (b) 400, (c) 500, and (d) 600 °C.

ZTO films at various annealing temperatures ranging from 300 to 600 °C. The surface morphology of the 300 °C-annealed ZTO film is rather rough, but the ZTO film annealed at 400 °C is much smoother. The rms roughness of the 400 °C-annealed ZTO film was 0.18 nm, which is much lower than 0.37 nm of the 300 °C-annealed film. Because the film density of the channel layer plays an important role in affecting the device performance and reliability, the densities of various ZTO thin films were evaluated by high-resolution XRR.[22] Figure 5 shows the XRR data for the ZTO films prepared at different annealing temperatures. The critical angle for total external reflection for the 600 °C-annealed ZTO film is higher than that for the 300 °C-annealed sample, indicating that the ZTO film annealed at 600 °C is denser than the 300 °C-annealed one (inset of Figure 5). The density of the ZTO films increased monotonously with increasing annealing temperature. The 300 °C-annealed sample had a density of 3.89 g/cm^3, whereas the density of the ZTO films annealed at 400, 500, and 600 °C increased to 4.30, 4.55, and 5.38 g/cm^3, respectively, as summarized in Table 1. The cation composition of the ZTO thin films remained unchanged with the annealing temperature (see Table 1).

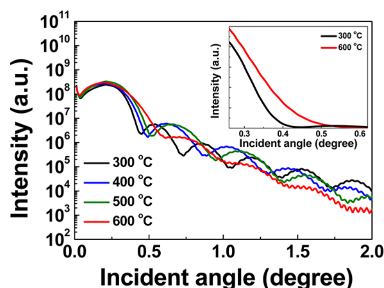

Figure 5. XRR data for the ZTO films prepared at various annealing temperatures.

Table 1. Roughness, Density, Thickness, and Cation Composition of a-ZTO Thin Films as a Function of the Annealing Temperature

annealing temperature (°C)	rms (nm)	density (g/cm^3)	thickness (nm)	Zn/(Zn + Sn)
300	0.37	3.89	8.83	0.49
400	0.18	4.30	6.84	0.51
500	0.18	4.55	6.30	0.51
600	0.21	5.38	6.65	0.51

Figure 6 shows the O 1s XPS spectra of the ZTO films annealed at 300−600 °C. The C 1s peak for C−C bonds was assigned to 284.5 eV to calibrate the photoelectron binding

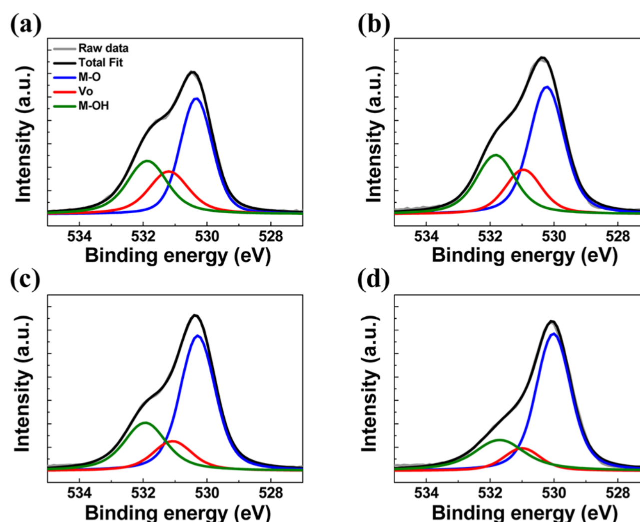

Figure 6. O 1s XPS spectra of the ZTO films annealed at (a) 300, (b) 400, (c) 500, and (d) 600 °C.

energy. The O 1s peak was deconvoluted into three peaks at 530.2, 531.2, and 531.9 eV. The O 1s peaks centered at 530.2 and 531.2 eV were assigned to oxygen atoms in the oxide lattice without and with oxygen vacancies, respectively. The peak at 531.9 eV was assigned to impurity-related oxygen, such as carbon and hydroxyl groups.[23] The area ratio of the peaks was used to estimate the relative quantities of the oxygen lattice, oxygen vacancy, and hydroxyl group, as summarized in Table 2.

Table 2. XPS O 1s Result for the Annealed ZTO Thin Films

annealing temperature (°C)	O 1s peak (eV)		
	lattice oxygen (O_O) (530.2 ± 0.16)	oxygen deficient (V_O) (531.2 ± 0.11)	hydroxyl (531.9 ± 0.12)
300	0.475	0.233	0.292
400	0.530	0.188	0.282
500	0.587	0.150	0.263
600	0.654	0.116	0.229

The relative areas of the hydroxyl-group-related peak and the oxygen-vacancy-related peak were reduced monotonically with increasing annealing temperature, as shown in Figure 6 and summarized in Table 2. In contrast, the relative area of the oxygen lattice peak increased with increasing annealing temperature.

Figure 7 shows the Cl 2p XPS spectra of the ZTO films at different annealing temperatures. The Cl 2p XPS spectra of all

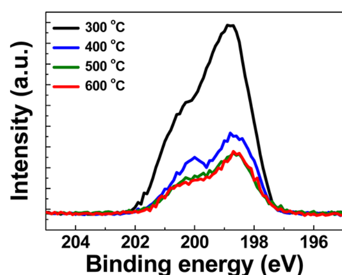

Figure 7. Cl 2p XPS spectra of the ZTO films at various annealing temperatures.

ZTO films show the coexistence of compounds, such as $ZnCl_n$ and $SnCl_n$. The concentration of Cl incorporated in the ZTO films decreased with increasing annealing temperature. The 300 °C-annealed ZTO film contained the largest concentrations of chlorine and hydroxyl groups (see Table 2). The incomplete decomposition of organic ligands and metal salts due to low annealing temperature is believed to cause the excessive incorporation of Cl ions and OH groups. In addition, the 300 °C-annealed ZTO films contain some pores or microvoids, as inferred from the rough surface and the lowest film density (3.89 g/cm^3). As the annealing temperature was increased, such impurities were reduced substantially with the enhanced decomposition and evaporation. Simultaneously, the hydroxyl groups (M−OH) were converted to oxides. As a result, the ZTO film became denser and the surface morphology improved with increasing annealing temperature.

The dependence of transfer characteristics ($I_{DS} - V_{GS}$) of the ZTO TFTs on the annealing temperature was examined. Figure 8 shows the representative transfer characteristics of the ZTO TFTs as a function of the annealing temperature. The field-effect mobility (μ_{FE}) was determined from the incremental

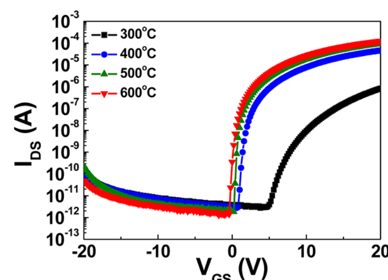

Figure 8. Representative transfer characteristics of the ZTO TFTs annealed at various temperatures.

slope of the $I_{DS}^{1/2}$ vs V_{GS} plot in the saturation region using the following equation:

$$I_{DS} = (WC_i/2L)\mu_{FE}(V_{GS} - V_{th})^2 V_{DS} \quad (1)$$

where L is the channel length, W is the width, and C_i is the gate capacitance per unit area. V_{th} was defined as the gate voltage that induces a drain current of $L/W \times 10$ nA at V_{DS} = 10.1 V. The subthreshold gate swing (SS = $dV_{GS}/d\log I_{DS}$ [V/decade]) was extracted from the linear part of the log(I_{DS}) vs V_{GS} plot. The 300 °C-annealed ZTO TFTs showed marginal performance: the μ_{FE}, SS, and $I_{on/off}$ ratio were 0.1 cm^2/(V s), 1.84 V/decade, and 3.1 × 10^5, respectively. In contrast, the 400 °C-annealed device exhibited reasonable transistor behavior. The μ_{FE}, V_{th}, SS, and $I_{on/off}$ ratio of the ZTO TFT annealed at 400 °C were 3.5 cm^2/(V s), 1.1 V, 0.36 V/decade, and 1.4 × 10^7, respectively, as listed in Table 3. Significant improvement in the device performance was observed for the ZTO TFTs annealed at 500 °C. The μ_{FE} and SS values for the 500 °C-annealed device were improved to 6.0 cm^2/(V s) and 0.28 V/decade, respectively. Moreover, the V_{th} value was reduced to nearly zero voltage (0.6 V) and the $I_{on/off}$ ratio was increased to 4.0 × 10^7, which is desirable for low power consumption of active matrix electronics. Further increase in the annealing temperature to 600 °C resulted in a higher μ_{FE} of 7.8 cm^2/(V s) and a lower SS of 0.25 V/decade. On the other hand, the V_{th} value deteriorated slightly to 0.11 V.

The SS value of a given TFT device is related to the total density of traps, including the bulk (N_{SS}) and semiconductor−insulator interfacial traps (D_{it}), according to the following equation:[24]

$$SS = \frac{qk_BT(N_{SS}t_{ch} + D_{it})}{C_i \log(e)} \quad (2)$$

where q is the electron charge, k_B is Boltzmann's constant, T is the absolute temperature, and t_{ch} is the channel layer thickness. N_{SS} and D_{it} in the ZTO TFTs were calculated by setting one of the parameters to zero. In this study, the N_{SS} and D_{it} values correspond to the maximum trap density formed in a given system. The $N_{SS,max}$ values for the 300-, 400-, 500-, and 600 °C-annealed devices were 7.2 × 10^{18}, 1.8 × 10^{18}, 1.6 × 10^{18}, and 1.4 × 10^{18} cm^{-2} eV^{-1}, respectively (see Table 3). This result suggests that higher annealing temperature can reduce the total trap density of the ZTO semiconductor and interfaces significantly.

The effects of annealing temperature on the dark NBS instability of the resulting ZTO transistors were investigated. The devices were stressed under the following conditions: V_{GS} and V_{DS} at −20 and 10.1 V, respectively, at room temperature and a stress duration of 4000 s. Figure 9 shows the evolution of

Table 3. Comparison of the Device Parameters Including μ_{FE}, SS, V_{th}, $I_{on/off}$, $D_{it,max}$, and $N_{ss,max}$ of the Various ZTO TFTs

annealing temperature (°C)	μ_{FE} (cm^2/(V s))	SS (V/decade)	V_{th} (V)	$I_{on/off}$	$D_{it,max}$ (eV^{-1} cm^{-2})	$N_{ss,max}$ (eV^{-1} cm^{-2})
300	0.1	1.84	7.34	3.1×10^5	6.4×10^{12}	7.2×10^{18}
400	3.5	0.36	1.10	1.4×10^7	1.2×10^{12}	1.8×10^{18}
500	6.0	0.28	0.58	4.0×10^7	9.7×10^{11}	1.6×10^{18}
600	7.8	0.25	0.11	1.0×10^8	8.7×10^{11}	1.4×10^{18}

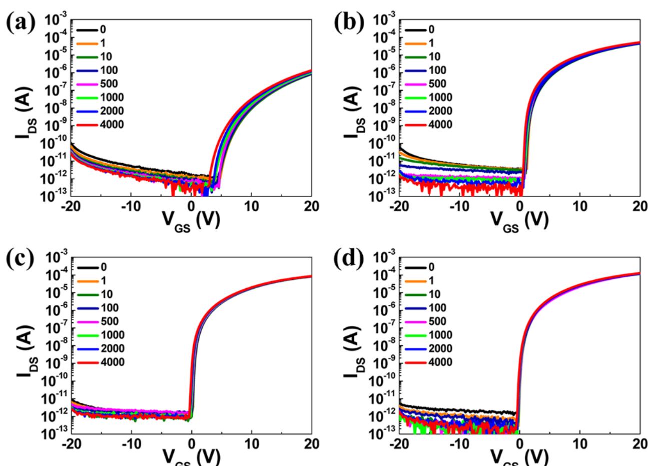

Figure 9. Evolution of the transfer characteristics of ZTO annealed at (a) 300, (b) 400, (c) 500, and (d) 600 °C as a function of the dark NBS time.

the transfer characteristics of the various ZTO TFTs as a function of the NBS time. A parallel V_{th} shift by −1.8 V after NBS was observed for the 300 °C-annealed device without a significant change in SS value, suggesting that V_{th} degradation originates from charge trapping rather than the creation of defects within the ZTO semiconductor. Higher temperature annealing of ZTO films improved the NBS stability of the resulting TFTs. The V_{th} shifts for 400, 500, and 600 °C-annealed devices were reduced to −0.60, −0.45, and −0.21 V, respectively. For a better understanding of NBS induced charge trapping, the relaxation times for all devices were extracted using the following stretched-exponential formula:[25]

$$\Delta V_{th}(t) = V_0\left\{1 - \exp\left[-\left(\frac{t}{\tau}\right)^{\beta}\right]\right\}, \qquad V_0 = V_g - V_{th,0} \tag{3}$$

where t is the time, τ is the relaxation time constant, β is the dispersion parameter, and $V_{th,0}$ is V_{th} before stress. Figure 10 shows the time dependence of ΔV_{th} for all the devices, which

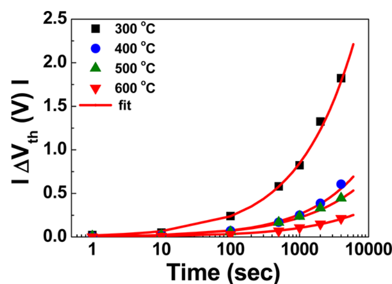

Figure 10. Dark NBS time dependence of ΔV_{th} for the various ZTO TFTs. The measured data was fitted to a stretched-exponential equation with a fitting parameter of τ and β.

were fitted to a stretched-exponential equation. For the 300 °C-annealed device, τ and β were 4.3×10^5 s and 0.50, respectively, as shown in Figure 10 and Table 4. The β values (0.50−0.55)

Table 4. Comparison of the Relaxation Time (τ) and Dispersion Parameter (β) at Room Temperature for the Various ZTO TFTs

stress condition	annealing temperature (°C)	τ @ RT (s)	β
NBS	300	4.3×10^5	0.50
	400	2.6×10^6	0.55
	500	9.0×10^6	0.49
	600	4.1×10^7	0.49
NBIS	300	5.7×10^3	0.78
	400	4.0×10^4	0.61
	500	1.1×10^5	0.59
	600	2.0×10^5	0.65

of all devices were independent of the annealing temperature, suggesting that the charge trapping mechanism responsible for the negative V_{th} shift is identical. On the other hand, the τ values for the ZTO TFTs increased dramatically with increasing annealing temperature, as shown in Figure 10 and Table 4. For example, the relaxation time for the 500 °C-annealed device was 9.0×10^6 s, which is 1 order of magnitude higher than that of the 300 °C-annealed device. The light-enhanced NBS instability is a critical issue, as mentioned earlier, because the optoelectronic devices including the transparent display are inevitably exposed to light illumination. Therefore, the NBIS instability of the soluble ZTO TFTs was also examined. The ZTO channel was irradiated with light (~2.0 mW/cm^2) at a wavelength of ~500 nm, which was filtered from a white-light halogen lamp. The applied V_{GS} and V_{DS} stress were identical to the dark NBS condition. Figure 11 shows the

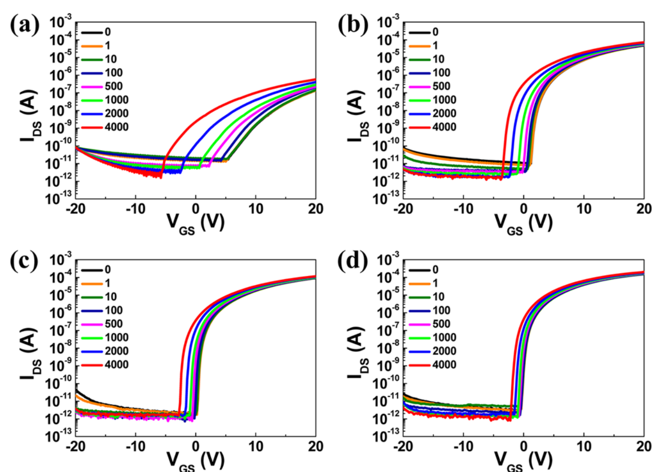

Figure 11. Evolution of the transfer characteristics of ZTO annealed at (a) 300, (b) 400, (c) 500, and (d) 600 °C as a function of the NBIS time.

dx.doi.org/10.1021/am400110y | ACS Appl. Mater. Interfaces 2013, 5, 3255−3261

evolution of the transfer characteristics as a function of the NBIS time for various ZTO TFTs. Light illumination of the ZTO channel region further accelerates the NBS-induced V_{th} shift. The 300 °C-annealed device suffered from a huge V_{th} shift of −10.5 V (Figure 11a). A similar trend was observed in that the NBIS instability of the ZTO TFTs also decreased with increasing annealing temperature. Therefore, a negative V_{th} shift was diminished significantly to 4.5 V for the ZTO TFT annealed at 400 °C (Figure 11b). The photobias stability was improved further by higher temperature annealing of 500 and 600 °C: the devices showed a negative V_{th} displacement of only 2.9 and 1.7 V shift, respectively (Figure 11c and d). To obtain insight into the V_{th} degradation mechanism by NBIS, the τ and β values were extracted for the NBIS time-dependent V_{th} instability using the same stretched-exponential formula, as shown in Figure 12. The β values (0.59−0.78) extracted for

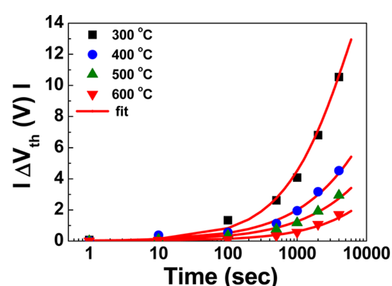

Figure 12. NBIS time dependence of ΔV_{th} for the various ZTO TFTs.

NBIS instability were higher than those for NBS instability, and the relaxation times were reduced significantly to 5.7×10^3 to 2.0×10^5 s, as summarized in Table 4. This suggests that the NBS and NBIS instabilities have different physical origins.

The negative V_{th} shift in the NBIS condition can be attributed to (1) photoionization of pre-existing neutral oxygen vacancy,[26,27] (2) trapping of photocreated hole carriers,[28] and (3) ambient interaction.[29] The latter mechanism of (3) can be excluded because the ZTO channel layers were encapsulated by PMMA. In the oxygen vacancy model, the two electrons can be photoexcited from neutral oxygen vacancies in the conduction band [$V_O \rightarrow V_O^{2+} + 2e^-$], leading to a negative V_{th} shift [so-called persistent photoconductivity (PPC)]. According to the electronic calculation, the V_O^{2+} state in ZnO-based materials is preferred over the V_O state due to its low formation energy when the Fermi energy is near the valence band maximum.[30] Therefore, the transition from V_O to V_O^{2+} can also be caused by lowering of the quasi Fermi energy, which corresponds to the application of NBS to TFTs. Or the migration of positively charged oxygen vacancy by negative bias applied to the gate electrode can induce negative free carriers in the channel, leading to the same negative V_{th} shift.[31] Therefore, the oxygen-vacancy-related model is responsible for the dark NBS and NBIS induced degradation. Obviously, the V_{th} deterioration accelerated by NBIS originates from the additional photo-ionization process of neutral V_O defects.

The trapping of photocreated hole carriers also plays an important role in the NBIS condition. During the NBIS condition, electron−hole pairs in the channel region are generated by light. The photocreated hole carriers move toward the gate dielectric by the NBS and become trapped at the interfacial trap states, causing a negative V_{th} shift.[28] However, this is not the case for the dark NBS condition because the number of existing hole carriers under the dark NBS condition would be extremely small due to a huge subgap density of states (10^{20} cm^{-3}) near the valence band of ZnO-based material.[32] This disparity can result in different β values between NBS and NBIS instability. The strong annealing temperature dependence on the NBS and NBIS instability of the ZTO TFTs can be understood on the basis of the mechanisms discussed. The inferior instability of the 300 °C-annealed device is related to the concentration of largest V_O and impurities in the ZTO channel layer (Figures 6 and 7). The negative V_{th} shift is enhanced by the PPC effect because V_O defects are potential donors. Or hole carrier trapping can also be responsible for this deterioration. The V_{th} instability by the hole carrier trapping is proportional to the number of holes generated by the applied bias and the number of trapping sites. The 300 °C-annealed ZTO channel showed the largest level of OH and Cl incorporation. This contamination may act as a generation center for hole carriers upon photon irradiation into the ZTO channel region. A similar adverse effect of Cl incorporation in the channel layer was also reported for vacuum-derived metal oxide TFTs.[33] Therefore, the inferior stability of the 300 °C-annealed device is attributed to a large amount of impurities and oxygen vacancy in the ZTO film as confirmed by XPS and XRR results. The improvement in the photobias stability of the ZTO TFTs annealed at 400 and 500 °C was attributed to the reduced oxygen vacancies and higher purity in the channel layer. Similar results were reported, which supports this observation.[3,34] The 600 °C-annealed device exhibited the best performance and reliability, which is consistent with its lowest V_O and impurity concentration. On the other hand, the partial crystallization of the channel layer at 600 °C can also be partially responsible for this improvement because the crystalline ZTO film has the lower distribution of tail states in the forbidden band gap. For practical application, an annealing temperature less than 500 °C is desirable considering the softening point of the glass substrate.

Finally, it is important to discuss how the annealing temperature can be lowered (<250 °C) to make it compatible with plastic substrates. To obtain a high quality film at low temperature, advanced annealing processes, such as high pressure oxygen annealing[35] or photo annealing,[23] can be viable approaches, since they effectively reduce the structural impurities in the channel layer and facilitate film densification at low temperature.

4. CONCLUSION

The effect of the annealing temperature on the device performance and photo bias instability of solution-processed ZTO TFTs was studied. Device performance of the ZTO TFTs was improved by increasing the annealing temperature. The 500 °C-annealed device exhibited a high μ_{FE}, low SS, V_{th}, and good $I_{on/off}$ ratio of 6.0 cm^2/(V s), 0.28 V/decade, 0.6 V, and 4.0×10^7, respectively, whereas the 300 °C-annealed ZTO TFTs showed marginal performance: the μ_{FE}, SS, and $I_{on/off}$ ratio were 0.1 cm^2/(V s), 1.84 V/decade, and 3.1×10^5, respectively. The dark NBS and NBIS instabilities for the ZTO TFTs depend strongly on the annealing temperature. The strong suppression of NBIS instability was also observed for the 500 °C-annealed ZTO device. The ΔV_{th} of the 500 °C-annealed ZTO device after the application of NBIS was reduced substantially from −10.5 V for the 300 °C-annealed device to −2.9 V. The dynamics of V_{th} shift with NBS and NBIS time for all ZTO TFTs was analyzed on the basis of the stretched exponential relaxation to improve the understanding

of stress time-dependent charge trapping. The τ values extracted from the 300 °C-annealed device under NBS and NBIS conditions were 4.3×10^5 and 5.7×10^3, respectively. In contrast, the 500 °C-annealed device exhibited τ values of 9.0×10^6 and 1.1×10^5, under NBS and NBIS conditions, respectively. This improvement can be explained by the photocreated hole trapping model and V_O transition model. In-depth analyses of the structural and chemical properties of ZTO films revealed that the purification and densification of the solution-processed ZTO channel layer are critical factors for high performance oxide TFTs with excellent photobias stability.

AUTHOR INFORMATION

Corresponding Author

*E-mail: jkjeong@inha.ac.kr (J.K.J.); thinfilm@snu.ac.kr (H.J.K.).

Notes

The authors declare no competing financial interest.

ACKNOWLEDGMENTS

This study was supported by a Korea Science and Engineering Foundation (KOSEF) grant funded by the Korean government (MEST) (No. R17-2008-043-01001-0 and No. 2012R1A2A2A02005854) and Inha University Research Grant and World Class University program through the Korea Science and Engineering Foundation funded by the Ministry of Education, Science and Technology (R31-2008-000-10075-0).

REFERENCES

(1) Nomura, K.; Ohta, H.; Takagi, A.; Kamiya, T.; Hirano, M.; Hosono, H. *Nature* **2004**, *432*, 488−492.
(2) Chiang, H. Q.; Wager, J. F.; Hoffman, R. L.; Jeong, J.; Keszler, D. A. *Appl. Phys. Lett.* **2005**, *86*, 013503.
(3) Yang, B. S.; Huh, M. S.; Oh, S.; Lee, U. S.; Kim, Y. J.; Oh, M. S.; Jeong, J. K.; Hwang, C. S.; Kim, H. J. *Appl. Phys. Lett.* **2011**, *98*, 122110.
(4) Heo, J.; Kim, S. B.; Gordon, R. G. *Appl. Phys. Lett.* **2012**, *101*, 113507.
(5) Gorrn, P.; Holzer, P.; Riedl, T.; Kowalsky, W.; Wang, J.; Weimann, T.; Hinze, P.; Kipp, S. *Appl. Phys. Lett.* **2007**, *90*, 063502.
(6) Banger, K. K.; Yamashita, Y.; Mori, K.; Peterson, R. L.; Leedham, T.; Rickard, J.; Sirringhaus, H. *Nat. Mater.* **2011**, *10*, 45−50.
(7) Kim, D.; Koo, C. Y.; Song, K.; Jeong, Y.; Moon, J. *Appl. Phys. Lett.* **2009**, *95*, 103501.
(8) Choi, C. G.; Seo, S. J.; Bae, B. S. *Electrochem. Solid-State Lett.* **2008**, *11*, H7−H9.
(9) Kim, M. G.; Kim, H. S.; Ha, Y. G.; He, J.; Kanatzidis, M. G.; Facchetti, A.; Marks, T. J. *J. Am. Chem. Soc.* **2010**, *132*, 10352−10364.
(10) Chipman, A. *Nature* **2007**, *449*, 131.
(11) Chang, Y. J.; Lee, D. H.; Herman, G. S.; Chang, C. H. *Electrochem. Solid-State Lett* **2007**, *10*, H135−H138.
(12) Jeong, S.; Jeong, Y.; Moon, J. *J. Phys. Chem. C* **2008**, *112*, 11082−11085.
(13) Seo, S. J.; Choi, C. G.; Hwang, Y. H.; Bae, B. S. *J. Phys. D: Appl. Phys.* **2008**, *42*, 035106.
(14) Park, S. K.; Kim, Y. H.; Kim, H. S.; Han, J. I. *Electrochem. Solid-State Lett.* **2009**, *12*, H256−H258.
(15) Jeong, Y.; Song, K.; Kim, D.; Koo, C. Y.; Moon, J. *J. Electrochem. Soc.* **2009**, *156*, H808−H812.
(16) Seo, S. J.; Yang, S.; Ko, J. H.; Bae, B. S. *Electrochem. Solid-State Lett.* **2011**, *14*, H375−H379.
(17) Jeong, S.; Ha, Y. G.; Moon, J.; Facchetti, A.; Marks, T. J. *Adv. Mater.* **2010**, *22*, 1346−1350.
(18) Meyers, S. T.; Anderson, J. T.; Hung, C. M.; Thompson, J.; Wager, J. F.; Keszler, D. A. *J. Am. Chem. Soc.* **2008**, *130*, 17603−9.
(19) Ong, B. S.; Li, C.; Li, Y.; Wu, Y.; Loutfy, R. *J. Am. Chem. Soc.* **2007**, *129*, 2750−1.
(20) Zhao, Y.; Duan, L.; Dong, G.; Zhang, D.; Qiao, J.; Wang, L.; Qiu, Y. *Langmuir* **2013**, *29*, 151−7.
(21) Kovacheva, D.; Petrov, K. *Solid State Ionics* **1998**, *109*, 327−332.
(22) Jeong, J. H.; Yang, H. W.; Park, J. S.; Jeong, J. K.; Mo, Y. G.; Kim, H. D.; Song, J.; Hwang, C. S. *Electrochem. Solid-State Lett.* **2008**, *11*, H157−H159.
(23) Kim, Y. H.; Heo, J. S.; Kim, T. H.; Park, S.; Yoon, M. H.; Kim, J.; Oh, M. S.; Yi, G. R.; Noh, Y. Y.; Park, S. K. *Nature* **2012**, *489*, 128−32.
(24) Greve, D. W. *Field Effect Devices and Applications: Devices for Portable, Low-power, and Imaging Systems*, 1st ed.; Prentice Hall: Englewood Cliffs, NJ, 1998; p 87.
(25) Deane, S. C.; Wehrspohn, R. B.; Powell, M. J. *Phys. Rev. B: Condens. Matter Mater. Phys.* **1998**, *58*, 12625−12628.
(26) Chowdhury, M. D. H.; Migliorato, P.; Jang, J. *Appl. Phys. Lett.* **2010**, *97*, 173506.
(27) Ji, K. H.; Kim, J. I.; Jung, H. Y.; Park, S. Y.; Choi, R.; Kim, U. K.; Hwang, C. S.; Lee, D.; Hwang, H.; Jeong, J. K. *Appl. Phys. Lett.* **2011**, *98*, 103509.
(28) Ji, K. H.; Kim, J. I.; Mo, Y. G.; Jeong, J. H.; Yang, S.; Hwang, C. S.; Park, S. H. K.; Ryu, M. K.; Lee, S. Y.; Jeong, J. K. *IEEE Electron Device Lett.* **2010**, *31*, 1404−1406.
(29) Yang, S.; Ji, K. H.; Kim, U. K.; Hwang, C. S.; Park, S. H. K.; Hwang, C. S.; Jang, J.; Jeong, J. K. *Appl. Phys. Lett.* **2011**, *99*, 102103.
(30) Janotti, A.; Van de Walle, C. G. *Rep. Prog. Phys.* **2009**, *72*, 126501−126530.
(31) Oh, H.; Yoon, S. M.; Ryu, M. K.; Hwang, C. S.; Yang, S.; Park, S. H. K. *Appl. Phys. Lett.* **2010**, *97*, 183502.
(32) Nomura, K.; Kamiya, T.; Yanagi, H.; Ikenaga, E.; Yang, K.; Kobayashi, K.; Hirano, M.; Hosono, H. *Appl. Phys. Lett.* **2008**, *92*, 202117.
(33) Kwon, J. Y.; Son, K. S.; Jung, J. S.; Lee, K. H.; Park, J. S.; Kim, T. S.; Ji, K. H.; Choi, R.; Jeong, J. K.; Koo, B. *Electrochem. Solid-State Lett.* **2010**, *13*, H213−H215.
(34) Jeong, Y.; Bae, C.; Kim, D.; Song, K.; Woo, K.; Shin, H.; Cao, G.; Moon, J. *ACS Appl. Mater. Interfaces* **2010**, *2*, 611−615.
(35) Rim, Y. S.; Jeong, W. H.; Kim, D. L.; Lim, H. S.; Kim, K. M.; Kim, H. J. *J. Mater. Chem.* **2012**, *22*, 12491−12497.